



Simultaneously enhanced piezoelectricity and curie temperature in BiFeO₃-based high temperature piezoelectrics

Jie Wu ^{a,b,1}, Gaochao Zhao ^{a,b,1}, Chengbing Pan ^{a,b}, Peng Tong ^a, Jie Yang ^a, Xuebin Zhu ^a, Lihua Yin ^{a,*}, Wenhui Song ^{a,*}, Yuping Sun ^{c,a,d}

^a Key Laboratory of Materials Physics, Institute of Solid State Physics, Chinese Academy of Sciences, Hefei, 230031, People's Republic of China

^b University of Science and Technology of China, Hefei, 230026, People's Republic of China

^c High Magnetic Field Laboratory, Chinese Academy of Sciences, Hefei, 230031, People's Republic of China

^d Collaborative Innovation Center of Advanced Microstructures, Nanjing University, Nanjing, 210093, People's Republic of China

ARTICLE INFO

Keywords:

Piezoelectricity

BiFeO₃

High curie temperature

High depolarization temperature

ABSTRACT

We report the structure, dielectric, ferroelectric and piezoelectric properties of Cr-Mn co-doped (1-y) BiFe_{1-x}Cr_xO₃-yBaTi_{1-x}Mn_xO₃ (0≤x≤0.04, 0.2≤y≤0.27) ceramics. By varying both x and y, a series of samples near morphotropic phase boundaries exhibiting both high ferroelectric Curie temperature T_C (~580–643 °C) and relatively large piezoelectric constant d_{33} are constructed. Especially, the sample with y = 0.24 and x = 0.02 is found to show coexistence of high depolarization temperature T_d (~551 °C) and relatively large d_{33} ~116 pC/N, superior to most of those of BiFeO₃ based high-temperature piezoceramics reported previously. The enhanced ferroelectric T_C in the Cr-Mn modified samples can be ascribed to the combined effects of large lattice distortion and high tetragonal phase content. These results demonstrate that constructing morphotropic phase boundaries via considering simultaneously the role of lattice distortion might be effective route to realize high-temperature and high piezoelectricity in BiFeO₃-based systems.

1. Introduction

As functional materials, piezoelectric materials have attracted considerable attention and are widely employed in electronic devices, due to the notable ability of converting between mechanical and electrical energy (and vice versa). So far, represented by Pb(Zr,Ti)O₃ (PZT) and relaxor-PbTiO₃ (PT) system, the lead-based piezoelectric materials have long been used in commercial area [1]. However, owing to toxic lead and environmental protection, the lead-free piezoelectric ceramics represented by BaTiO₃ (BTO), (K,Na)NbO₃ (KNN), BiFeO₃ (BFO) and (Bi_{0.5}Na_{0.5})TiO₃ (BNT) have received considerable attention and have been developed rapidly [2,3]. Recently high-temperature piezoelectric materials with high T_C have received increasing attention due to their potential applications in the fields of the aircraft, aerospace and nuclear power areas. Nevertheless, the relatively low Curie temperature T_C for KNN (T_C ~415 °C) and BTO (T_C ~120 °C), as well as the depolarization temperature (T_d) of approximately 160 °C for BNT could not meet the needs of high temperature applications (the operating temperature of 400–500 °C or greater) [4,5].

BFO with high FE Curie temperature (T_C ~827 °C) have also attracted increasing attention in the area of high-temperature piezoceramics [6]. For example, the T_C of the solid solution BiFeO₃-PbTiO₃ (BFO-PT) is high (~635 °C) [7]. Moreover, high T_C (~510 °C) and enhanced d_{33} are obtained in BFO-PT-(K_{1/2}Bi_{1/2})TiO₃ system [8]. On the other hand, lead-free (1-x)BiFeO₃-xBaTiO₃ (BFO-BTO) ceramics with relatively high piezoelectric performance and T_C are one of most promising materials for high-temperature applications. Generally, morphotropic phase boundaries (MPB) or polymorphic phase transition (PPT) play an important role in enhanced ferroelectric (FE) properties and excellent piezoelectric properties [9,10]. Although PPT is useful in achieving high piezoelectricity, it shows a strong temperature dependence, resulting in the unsatisfactory thermal depoling behavior [11]. On the other hand, piezoceramics near MPB do not suffer such strong temperature dependence. However, larger piezoelectric constant d_{33} values obtained in piezoceramics near MPB are often achieved at the cost of their FE T_C values [12]. In BFO-based ceramics maximum piezoelectric effect was usually observed near the MPB with coexisting rhombohedral (R) and tetragonal (T) phases [13–16]. For BFO-based piezoceramics, low T_d ,

* Corresponding authors.

E-mail addresses: lhyin@issp.ac.cn (L. Yin), whsong@issp.ac.cn (W. Song).

¹ Jie Wu and Gaochao Zhao are co-first authors.

<https://doi.org/10.1016/j.jeurceramsoc.2021.08.030>

Received 23 April 2021; Received in revised form 22 July 2021; Accepted 16 August 2021

Available online 18 August 2021

0955-2219/© 2021 Elsevier Ltd. All rights reserved.

high leakage current and low resistivity are still required to be resolved [6,17].

In the present work, we investigated the structural, dielectric, FE and piezoelectric properties of BFO-BTO ceramics via incorporating simultaneously Cr and Mn ions. Interestingly, the Cr-Mn modified samples are found to show coexistence of high T_d/T_C and relatively high piezoelectricity near MPB, whose possible origins were also discussed.

2. Experimental

$(1-y)\text{BiFe}_{1-x}\text{Cr}_x\text{O}_3\text{-}y\text{BaTi}_{1-x}\text{Mn}_x\text{O}_3$ (BFC-BTM) ($0 \leq x \leq 0.04$, $0.2 \leq y \leq 0.27$) ceramics were fabricated using the conventional solid-state method as reported previously [13]. For clarity, the samples with $y = 0.24$ and $x = 0.01$, or $y = 0.27$, $x = 0.03$, etc., will hereafter be abbreviated as $y0.24x0.01$, or $y0.27x0.03$, etc. Bi_2O_3 (99.5 %, Sinopharm Chemical Reagent Co Ltd., Shanghai, China), Fe_2O_3 (99 %, aladdin Co Ltd., Shanghai, China), Cr_2O_3 (99 %, aladdin Co Ltd., Shanghai, China), BaCO_3 (99.8 %, aladdin Co Ltd., Shanghai, China), TiO_2 (99.8 %, aladdin Co Ltd., Shanghai, China) and MnO_2 (99.9 % Alfa Aesar Co Ltd., Massachusetts, America) were used as the raw materials. The final sintering temperatures for all the samples were 950–980 °C for 2 h in air. For comparison of sintering atmosphere on the piezoelectric properties, the sample $y0.24x0.02$ was also sintered in O_2/N_2 atmosphere (the flow rate is 50/250 mL/min) at the same final sintering temperature. The room temperature (RT) X-ray diffraction (XRD) measurement was carried out with a Philips X'pert PRO x-ray diffractometer using $\text{Cu K}\alpha$ radiation. The crystal structures of the samples were

analyzed using a Rietveld refinement program based on the XRD results. The Raman scattering measurements were performed using a confocal microprobe Raman spectrometer (Renishaw Invia, 532 nm laser line). The FE polarization were measured by using a FE test system (Precision LC, Radian Technologies). Dielectric measurements were performed with a commercial LCR meter (TH2828S) at different frequencies (1–1000 kHz) ($300 \leq T \leq 1000$ K). The direct current (DC) resistivity as a function of temperature was measured by the two-probe method with a high-resistance meter (Keithley 6517B). The surface morphology analyses of the samples were carried out by a field-emission scanning electron microscopy (FE-SEM, FEI-designed Sirion 200, Hillsboro, OR). For the piezoelectric measurements, the samples were polarized at 30–100 °C in the silicone oil bath under a dc field of 50 kV/cm for 30 min. The poled samples were annealed at selected temperatures for one hour, and cooled down naturally. The piezoelectric coefficient d_{33} of the samples was measured by a quasi-static piezoelectric d_{33} -meter (ZJ-6).

3. Results and discussion

3.1. Structure

Figs. 1a-c and S1 show the RT powder XRD patterns of BFC-BTM ($0 \leq x \leq 0.04$, $0.2 \leq y \leq 0.27$) ceramics. All the samples show the perovskite structure without any impurities. As shown in Fig. 1b-c, for the $y = 0.24$ samples with varied x , the double peaks around the diffraction angle 2θ of 39 ° and 56 ° gradually merge into two single peaks,

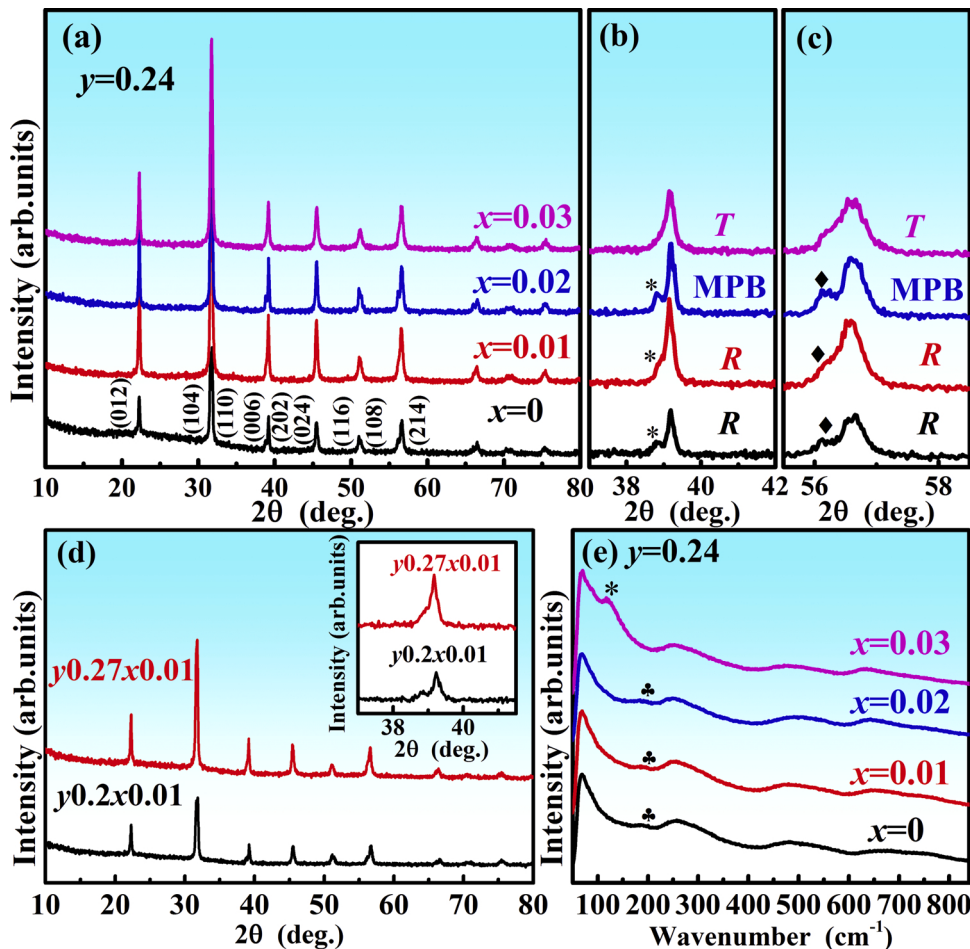


Fig. 1. (a) The RT XRD patterns and corresponding magnification around 2θ of (b) 39 ° and (c) 57 ° for the $y = 0.24$ samples. *, ◆ indicate the structure transition. (d) The RT XRD patterns for the representative samples near MPB with $y = 0.2$ and $y = 0.27$. Inset in (d) is the RT XRD patterns around 2θ of 39 ° for the $y0.27x0.01$ and $y0.2x0.01$ MPB samples. (e) RT Raman spectra for the $y = 0.24$ samples. *, ♦ indicate the characteristic peaks for R phase.

respectively, with x increasing above 0.03, demonstrating a structure transition from a R to T phase. Similarly, the $y = 0.2\text{--}0.27$ samples with various x also show a R to T phase transition with the MPB region at $x \sim 0.01$, as shown in Fig. 1d (see also Fig. S1).

The RT Raman spectra were also recorded to further check the structure transition in these samples, as shown in Figs. 1e and S2. The phonon mode at about 180 cm^{-1} disappears and a new phonon mode at about 130 cm^{-1} appears with $x \geq 0.03$ for $y = 0.24$, reminiscent of the La-doping induced R to T structural transition in $\text{Bi}_{1-x}\text{La}_x\text{FeO}_3$ system [18] and consistent with the XRD results shown in Fig. 1a-c. Similar variation in the Raman spectra with increasing x were also observed near the phase transition in the series of samples with $y = 0.2$ and 0.27 (Fig. S2).

3.2. The surface morphologies

Figs. 2 and S3-S4 show the typical SEM images for all samples with $y = 0.2\text{--}0.27$, which indicates a dense microstructure for all the samples. And the fresh fracture surface morphologies for the $y = 0.24$ samples and other MPB samples (the $y=0.2x0.01$ and $y=0.27x0.01$ samples) are shown in Fig. S5. Some small grains can be seen at the grain boundaries for both the natural surfaces and the fresh fracture surfaces of some of the samples. These small grains might arise from the abnormal grain recrystallization or impurities. The RT XRD with a higher resolution for these samples (shown in Fig. S6) also show no additional diffraction peaks due to impurities, which might be due to the rather low content of impurities or the absence of impurities. The dense microstructure is consistent with the high relative density obtained by the Archimedes principle for these samples, as listed in Table 1. The low relative density for $y0.2x0$ and $y0.24x0$ samples might be due to the relative low sintering temperature and easy evaporation of Bi_2O_3 [19]. The average grain sizes at the surface are determined from Nano Measurer software to be about 4.0, 3.6, 5.9, and $1.2\text{ }\mu\text{m}$ for the $y = 0.24$ samples with $x = 0$, 0.01, 0.02 and 0.03, respectively. On the other hand, the average grain sizes in the interior (see Fig. S5) are determined from Nano Measurer software to be about 4.2, 3.2, 4.9, and $1.2\text{ }\mu\text{m}$ for

the $y = 0.24$ samples with $x = 0$, 0.01, 0.02 and 0.03, respectively. There is no obvious difference of the grain size between at the surface and in the interior. And the decrease of the grain size in $x = 0.03$ sample (T phase) might be due to the change of sintering activity induced by structure transition. The lattice parameters and the unit cell volume V versus x for $y = 0.24$ samples obtained from the Rietveld refinements are plotted in Fig. S7. The abnormal variation of lattice parameters and V was found near the $R\text{-}T$ phase transition region. On the one hand, the diffusion coefficient D can be calculated from the formula: $D = D_0 \exp(-E/k_B T)$, where D_0 is the pre-exponential factor, k_B is the Boltzmann constant and E is the activation energy for the diffusion process [20]. Taking the activation energy E as equal to $\Delta h\text{-}\Delta s$, where Δh is the enthalpy and Δs is the entropy for atomic diffusion. And then the equation becomes $D = (v\lambda^2/6)\exp(\Delta s/k_B)\exp(-\Delta h/k_B T) = D_0 \exp(-\Delta h/k_B T)$. It has been shown that for a given class of materials, the value of D_0 are nearly constant. Moreover, the unit cell volume and lattice parameters of the two phases are different, thus there is an change in the activation energy, enthalpy and intrinsic diffusion coefficients of the two crystal lattices [21]. On the other hand, there are differences in the diffusion coefficients among different elements. Increasing the doping of chemical elements (such as Cr/Mn) also significantly affects the sintering process of ceramics and the grain growth rate (faster or slower), eventually resulting in a change of the grain size [22].

3.3. FE and dielectric properties

Figs. 3a and S8 show the RT polarization-electric field ($P\text{-}E$) hysteresis loops at 100 Hz for $y = 0.24$ and $y = 0.2\text{--}0.27$ samples with varied x , respectively. The remnant polarization P_r increases with increasing x , reaching a maximum near the MPB at $x = 0.02$, and then decreases dramatically at $x = 0.03$ in the T phase region. Fig. 3b,d show the temperature dependence of dielectric constant ($\epsilon'\text{-}T$) at 1 MHz for $y = 0.2\text{--}0.27$ samples with varied x , respectively. A sharp dielectric peak corresponding to the FE to paraelectric transition (T_C) in $\epsilon'\text{-}T$ was observed for all the samples. It is noted that in Fig. 3c there is not a consistent trend in the dielectric response as a function of x , whose trend

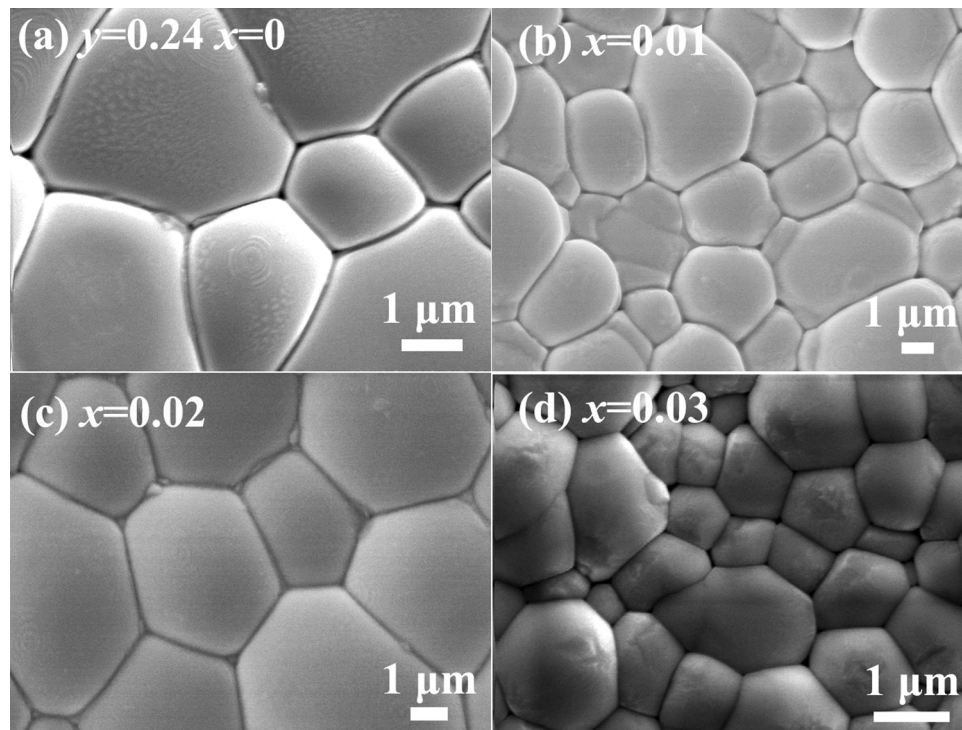


Fig. 2. The surface morphologies at the surface for all the $y = 0.24$ samples.

Table 1

RT dielectric constant ϵ_r and dielectric loss $\tan \delta$ (measured at 1 kHz), Curie (T_C) and depolarization (T_d) temperatures, piezoelectric constant d_{33} , relative density, remnant polarization (P_r), the average grain size d , activation energies E_a and the highest temperatures (T_h) for the resistivity higher than $\sim 1 \text{ M}\Omega \text{ cm}$ for BFC-BTM system.

Samples	ϵ_r	$\tan \delta$	T_C (°C)	T_d	d_{33}	relative density	P_r	d (μm)	E_a (eV)	T_h (°C)
y0.24x0	204	0.063	584		45	90.2%	13.3	4.0	0.77	164
y0.24x0.01	228	0.030	639	620	96	95.3%	13.8	3.6	1.11	315
y0.24x0.02	361	0.018	580	551	116	97.1%	16.2	5.9	1.08	270
y0.24x0.03	568	0.017	638		27	98.1%	3.9	1.2		
y0.27x0	459	0.035	557		86	91.0%	17.4	3.5	0.85	165
y0.27x0.01	628	0.030	550	515	135	97.8%	16.7	2.2	0.9	198
y0.2x0	252	0.056	645		26	88.1%	3.2	5.9	0.83	287
y0.2x0.01	679	0.049	643	589	80	95.7%	13.3	6.0	1.01	241

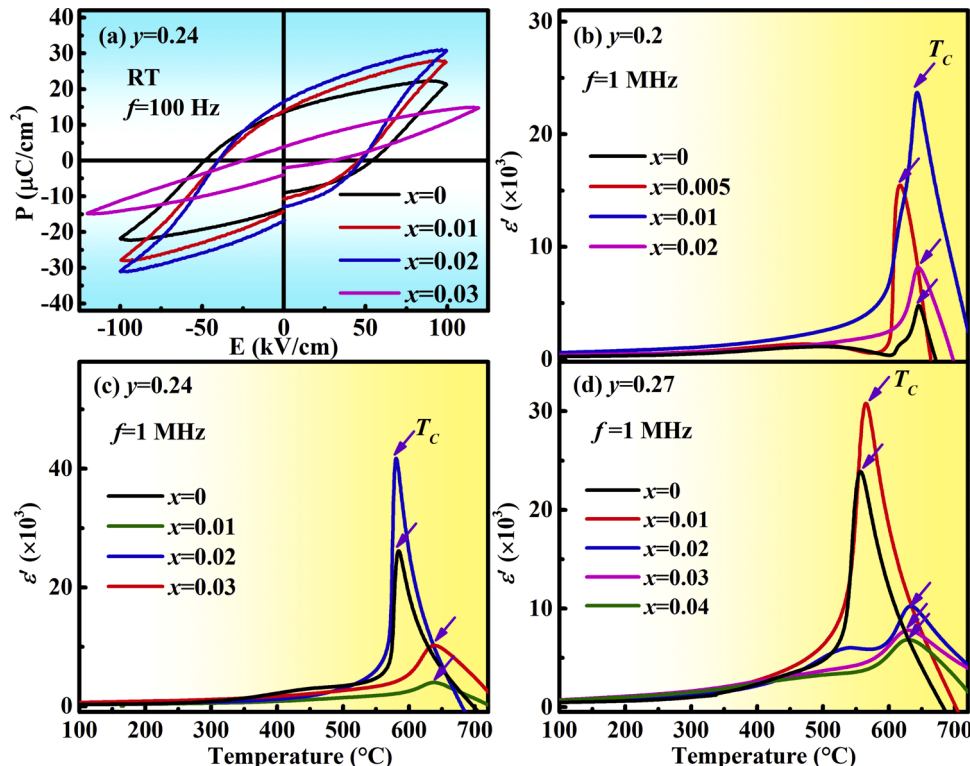


Fig. 3. (a) The RT P - E loops at $f = 100 \text{ Hz}$ for the $y = 0.24$ samples. The temperature dependence of dielectric constant ϵ' at $f = 1 \text{ MHz}$ for the (b) $y = 0.2$, (c) $y = 0.24$ and (d) $y = 0.27$ samples.

is closely related to the crystal structure and the variation of lattice distortion. Moreover, the Cr-Mn content x dependent T_C for different y are also plotted in Fig. 4a. It is seen that all the Cr-Mn co-doped samples with $y = 0.24$ and 0.27 shows higher T_C than those of the samples with $x = 0$, except for the samples with $y = 0.2$. And the variation of T_C as a function of x also shows non-monotonic trend, as shown in Fig. 4a. Nearly all the samples in the T phase region show higher T_C than those in the R phase region except for $y0.24x0.01$ sample. The fact that T_C fluctuates with varied x in BFO-BTO system is related in general to the degree of lattice distortion induced by possible varied Mn ionic valence. [13] Larger lattice distortion implies a higher energy barrier for the phase transition and result in a higher T_C , which will be discussed later. In addition, a slight shoulder in is observed in the temperature range of $\sim 400\text{--}500$ °C below T_C in nearly all the samples, which might be related to the antiferromagnetic to paramagnetic phase transition coupled with Maxwell-Wagner effect [23,24]. The temperature dependence of dielectric constant (ϵ') at different frequencies for the $y = 0.24$ samples are shown Fig. S9. All these samples show a frequency independent dielectric peaks near T_C , indicating a FE behavior for all the samples. It is different from the transformation from a pseudocubic to R

phase accompanied by the formation of the relaxor FE state in other BFO-BTO compositions [25,26]. The P_r , T_C , ϵ_r , $\tan \delta$ are summarized in Table 1. It is noted that the dielectric loss $\tan \delta$ and dielectric constant ϵ_r increase with increasing x , respectively. The high conductivity and high dielectric loss in bulk BFO are usually due to oxygen vacancies and mixed $\text{Fe}^{2+}/\text{Fe}^{3+}$ valence states. And the improved DC resistivity is obtained in Mn-modified BFO-BTO ceramics, which possibly results from reduced content of oxygen vacancies owing to donor doping [23]. Incorporating simultaneously Cr and Mn ions did improve the dielectric property compared with the undoping $x = 0$ sample.

3.4. Electrical transport property

The resistivity versus temperature (ρ - T) plotted for the selected samples in the form of $\ln \rho - 1000/T$ are shown in Figs. 4b and 5a. All the samples show a gradual reduction in resistivity with increasing temperature. And the resistivity of these samples follows the thermally activated conduction (TAC) law, $\rho = \rho_0 \exp(E_a/k_B T)$, where E_a is the activation energy. The values of E_a for these samples are in the range of 0.76–1.12 eV shown in Fig. 5b and are close to that of oxygen vacancy

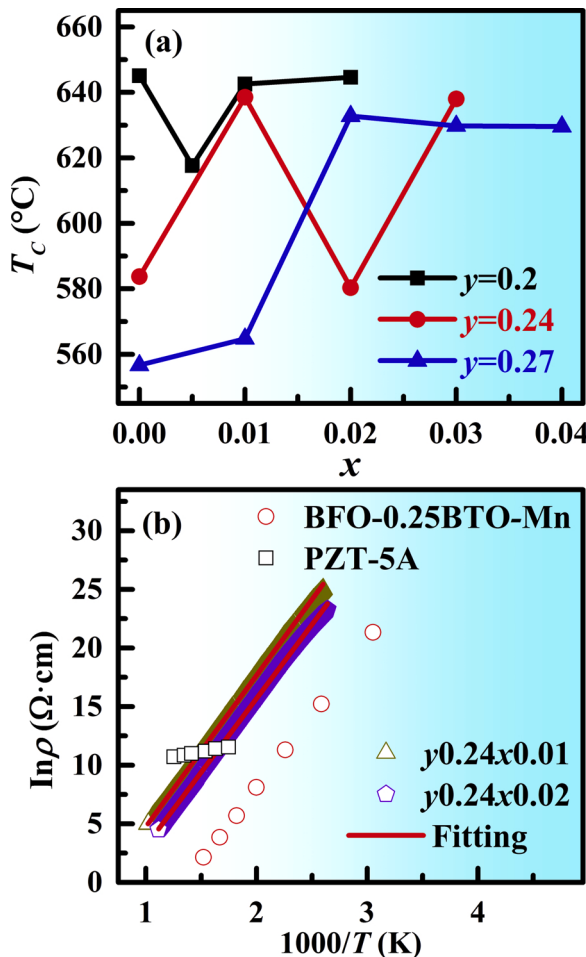


Fig. 4. (a) The Curie temperature T_C versus x for all samples. (b) The plots of $\ln \rho - 1000/T$ and the corresponding fitting according to the TAC law. Data for commercial PZT-5A ceramics and BFO-0.25BTO-Mn extracted from Ref. [23] is also shown here for comparison.

migration [27], indicating a close relationship between the increased electrical conduction at high temperature and the oxygen vacancies in these samples. It is noted that the values of E_a and resistivity for all the Cr-Mn co-doped samples are higher than those of the undoping samples ($x = 0$) and the highest resistivity is obtained in the samples $y0.24x0.01$ and $y0.24x0.02$. And for the $y0.24x0.01$ and $y0.24x0.02$ samples the resistivity is higher than $\sim 1 \text{ M}\Omega \text{ cm}$ below ~ 315 and 270°C , respectively. The highest temperatures (T_h) for the resistivity higher than $\sim 1 \text{ M}\Omega \text{ cm}$ for these samples are listed in Table 1. It is noted that high-temperature resistivity of the $y0.24x0.01$ and $y0.24x0.02$ samples is higher compared with BFO-0.25BTO-Mn and commercial PZT-5A ceramics [23], as shown in Fig. 4b. The higher DC resistivity and improved electric properties may be due to Cr-Mn doping induced the suppression of the formation of Fe^{2+} and reduction of oxygen vacancy concentration [23,28].

3.5. The piezoelectric properties

Fig. 6a-c show the piezoelectric coefficient d_{33} as a function of Cr-Mn content x for the three series of samples with different y . It is clear that maximum values of d_{33} are always obtained for the samples near MPB. These results indicate that the appropriate amount of Cr and Mn ions could enhance the piezoelectric properties, which can be ascribed to the more easily rotated polarization under applied electric fields at MPB [14]. In perovskite ferroelectrics, it is suggested that d_{33} can be expressed as $d_{33} \propto \varepsilon_r P_r$ [29]. Indeed, the $\varepsilon_r P_r$ show the similar trend as d_{33}

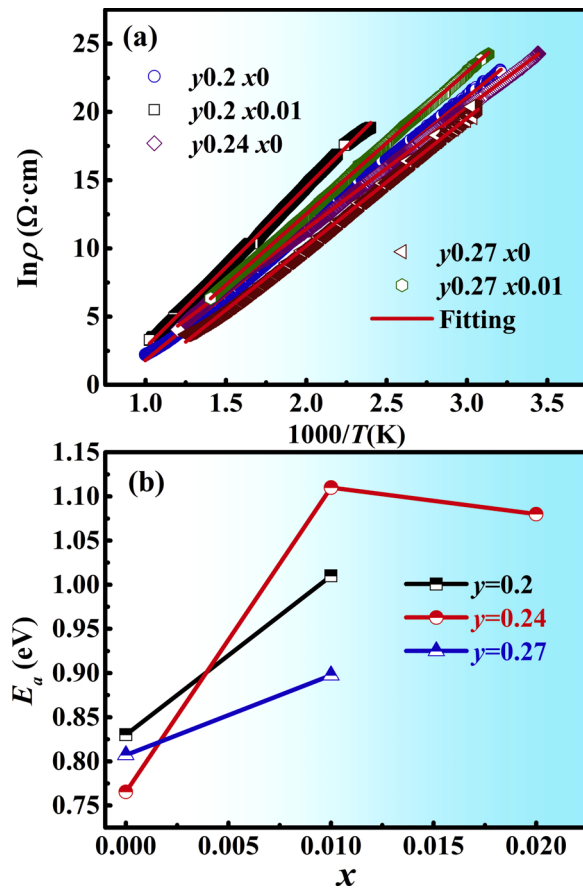


Fig. 5. (a) The plots of $\ln \rho - 1000/T$ and the corresponding fitting according to the TAC law for the selected samples. (b) Activation energies E_a as a function of x for the $y = 0.2$ - 0.27 samples.

with increasing x for the samples with $y = 0.2$ - 0.27 shown in Fig. 6a-c, confirming that improved FE and dielectric properties play an important role in the enhanced d_{33} . In ferroelectric ceramics both the intrinsic and extrinsic effects contribute to the piezoelectric coefficient. The intrinsic effect is dominated by the lattice distortion. And the extrinsic contributions are attributed to domain walls, defect dipoles and so on [30,31]. In ferroelectrics, P_r should directly reflect the degree of lattice distortion and directly related to the intrinsic properties [30]. For $y = 0.24$ samples, with increasing x , P_r reaching a maximum near the MPB at $x = 0.02$, and then decreases dramatically at $x = 0.03$ (as shown in Fig. 3a and Table 1). Moreover, ε_r is associated with the curvature of the free-energy density profile of perovskite ferroelectrics with respect to the polarization ($\partial^2 G / \partial P^2$) and sensitive to the crystal structure [32]. And ε_r increases monotonically with increasing x for $y = 0.24$ samples (see Table 1), consequently leading to the larger d_{33} . These results together with the matching trend between $\varepsilon_r P_r$ and d_{33} with increasing x , suggest that the intrinsic contribution dominates over the extrinsic contribution to the piezoelectricity in BFC-BTM system.

We summarize in Fig. 6d the excellent piezoelectric properties for non-textured lead-free piezoelectric ceramics, such as BTO [33], KNN [34,35], NBT [36,37], BFO [14,23,38-42], BiScO₃-PbTiO₃ (BSPT) [43], BFO-PT based ceramics [8,44,45], some bismuth layer-structured (BLS) ceramic oxides [46-48], and typical PZT ceramics [35]. It should be pointed out that d_{33} for perovskite ferroelectrics tend to be inversely proportional to T_C . Most of these materials show either relatively low T_C ($< 400^\circ\text{C}$) or low d_{33} ($< 20 \text{ pC/N}$). However, piezoceramics with T_C higher than 400°C and even exceeding 500°C and high operating temperatures (200°C - 580°C) are desired in practice [5,8]. All the BFO-BTO based piezoceramics both reported previously and studied in

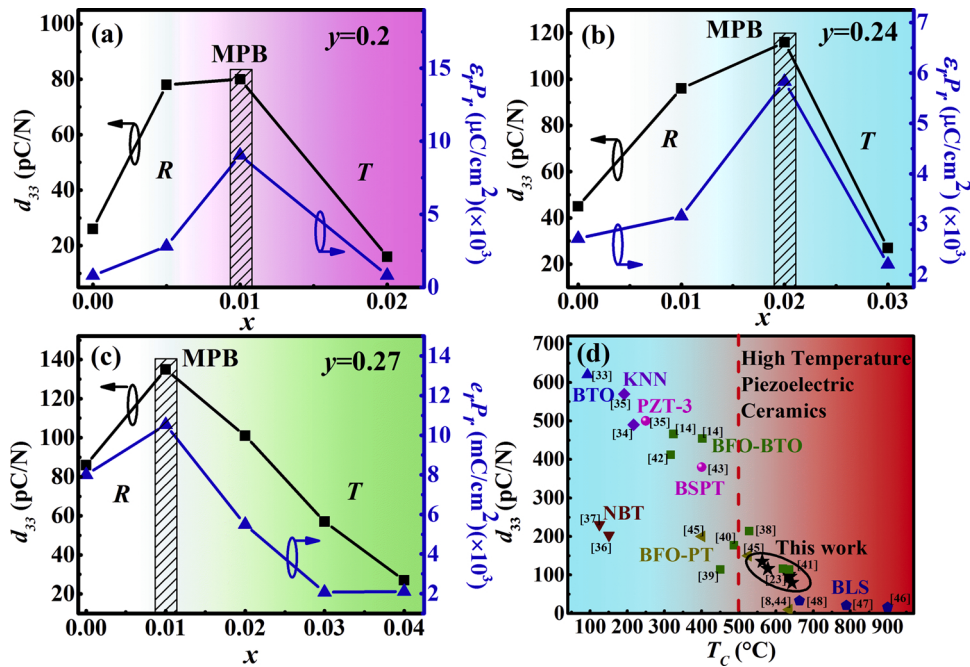


Fig. 6. d_{33} and $\epsilon_r P_r$ as a function of x in the (a) $y = 0.2$, (b) $y = 0.24$ and (c) $y = 0.27$ samples. (d) The previously reported d_{33} and T_c of some lead-based and lead-free based ceramics [8,14,23,33–48].

the present work exhibit both relatively high T_c (~450–619 °C) and large d_{33} (~116–402 pC/N). These results indicate that Cr/Mn-modified BFO-BTO based lead-free piezoelectric ceramics present potential candidates for high-temperature application.

Since the piezoelectricity usually deteriorates rapidly far below the Curie temperature T_c due to the depolarization, it is important to test the thermal stability of piezoelectricity. The poled samples were annealed at different temperatures, and the annealing temperature dependence of normalized d_{33} ($d_{33}-T$) for the selected samples are shown in Fig. 7. The

values of d_{33} gradually decrease with increasing temperature for all the samples. The $y0.24x0.02$ sample shows the best thermal stability of piezoelectricity and it keeps ~90 % of the initial RT piezoelectricity below ~400 °C and 70 % even at T_d ~551 °C near T_c . The d_{33} for $y0.24x0.02$ is non-zero even after annealed above T_c , which is also reported previously in other piezoceramics and might be due to the existence of short-range FE interaction above T_c [49]. However, d_{33} of other samples with similar T_c decreased to ~75–85% of the initial value of RT piezoelectricity at ~300 °C and then dropped dramatically above

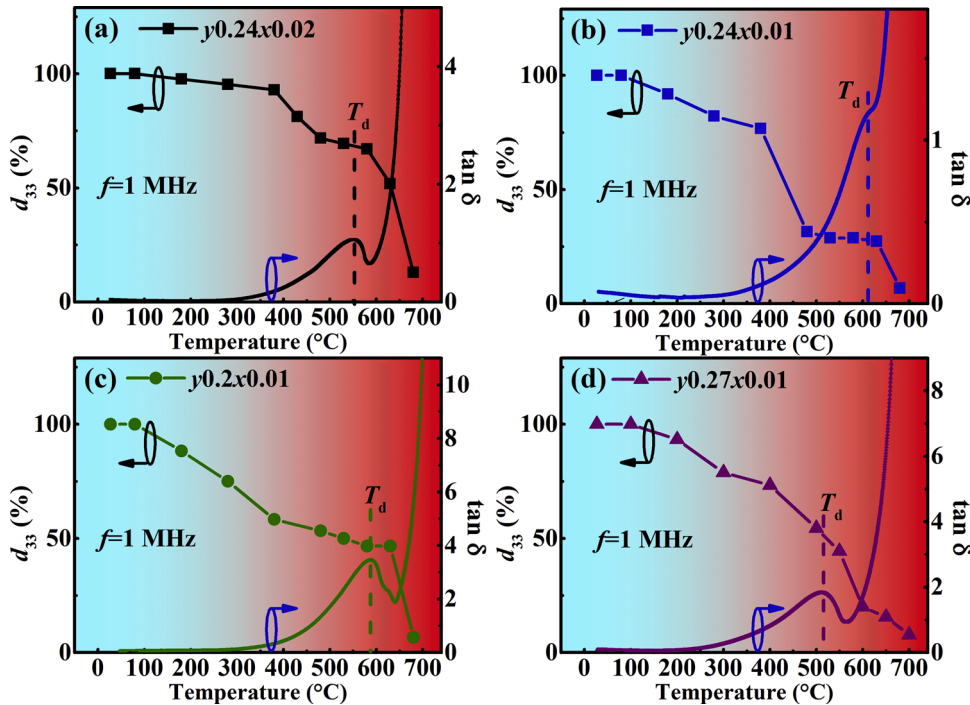


Fig. 7. The annealing temperature dependence of normalized d_{33} and temperature dependence of the dielectric loss for the (a) $y0.24x0.02$, (b) $y0.24x0.01$, (c) $y0.2x0.01$ and (d) $y0.27x0.01$ samples.

$T_d \sim 400$ °C. The dielectric loss ($\tan \delta$) versus temperature at $f = 1$ MHz for the selected samples are also plotted in Fig. 7. The peak near T_C of $\tan \delta-T$ curves can be also used to determine the depolarization temperature due to the fact that abnormally large loss can be induced by the substantially increased polarization fluctuation and domain wall motion at high temperature near T_C [49,50]. As can be seen in Fig. 7, the loss peak temperature are overall consistent with the T_d obtained from the $d_{33}-T$ data.

3.6. Discussion on the origin of enhanced T_C

Fig. 8a also displays the relationships between the T_d and T_C for the selected samples in this work as well as the BFO-BTO based piezoelectric ceramics reported previously [23,28,40–4251–59]. It is seen that our samples show higher T_d together with high T_C as compared with other BFO-BTO based piezoceramics. Especially, the $y0.24x0.02$ sample shows a coexistence of high $T_d \sim 580$ °C and relatively large $d_{33} \sim 116$ pC/N.

Now let's discuss the possible origin of the enhanced T_C in the Cr-Mn modified samples. Fig. 8b shows the y dependent R distortion (characterized by $90-\alpha_R$) and tolerance factor ($t = \frac{R_A+R_O}{\sqrt{2}(R_B+R_O)}$) by fixing $x = 0$ for the samples lying in the R phase region. As can be seen, the FE T_C increases monotonously with increasing R distortion or decreasing tolerance factor t , which is consistent with previous reports in other perovskites [60]. Larger R distortion implies a higher energy barrier for $R-C$ phase transition and hence a higher T_C . This result indicates the importance of lattice distortion in the increasing of FE T_C . On the other hand, it is also noted that the sample $y0.24x0.02$ near MPB shows the abnormal lower T_C than those of the samples $y0.24x0.01$ and $y0.24x0.03$. Since piezoelectric as well as FE properties of the samples near MPB is very sensitive to the crystal structure [25] and hence to the oxygen vacancies, we studied the effect of sintering atmosphere on the structures and FE T_C for the sample $y0.24x0.02$. The dielectric data ($\epsilon'-T$) shows that the FE T_C increases significantly for the sample sintered in O_2 compared with the one sintered in air (at same sintering temperature), as shown in Fig. 8c. The RT dielectric loss value (Measured at 1 kHz) of the $y0.24x0.02$ sample annealed in oxygen (~ 0.004) is much smaller than that of the sample annealed in air (~ 0.018 , shown in Table 1), which is related to reduced content of oxygen vacancies. However, comparing with the sample sintered in air, the T_C also increases slightly

for the one sintered in N_2 accompanied by the increase of RT dielectric loss (~ 0.104 , measured at 1 kHz), which is related to increased content of oxygen vacancies. And the decrease of the characteristic XRD peaks near 39 ° and 56 ° for the R -phase indicates a reduction of R -phase ratio in the sample sintered in O_2 and N_2 (Fig. 8d and inset in it). Detailed refinement of the XRD patterns shown in Fig. 9 for the three samples shows indeed an increase of T phase ratio from 32 % for the sample sintered in air to 54 % and 60 % for the one in N_2 and O_2 , respectively. Furthermore, it is also found that nearly all the samples in the T phase region with tetragonal distortion show higher T_C than those in the R phase region (except $y0.24x0.01$). These results seem to imply a significant role of the lattice distortion as well as the tetragonal phase ratio in obtaining high T_C in the BFO-based piezoceramics.

4. Conclusions

In summary, the crystal structure, dielectric, FE, and piezoelectric properties of $(1-y)BiFe_{1-x}Cr_xO_3-yBaTi_{1-x}Mn_xO_3$ (BFC-BTM, $0 \leq x \leq 0.04$, $0.2 \leq y \leq 0.27$) ceramics were investigated. Interestingly, both enhanced piezoelectricity and T_C were observed in this system. The Cr-Mn codoping was found to effective in obtaining relatively large d_{33} (~ 96 – 135 pC/N) and high T_C (~ 580 – 643 °C) in the BFO-BTO-based system. Especially, coexistence of high depolarization temperature T_d (~ 551 °C) and relatively large $d_{33} \sim 116$ pC/N, superior to most of those of BFO-based high-temperature piezoceramics reported previously, were observed in the sample $y0.24x0.02$. The origin of enhanced FE T_C in the Cr-Mn modified samples was discussed based on the lattice distortion and tetragonal phase ratio. Our results demonstrate that constructing MPB via considering simultaneously the role of lattice distortion might be important in achieving both high T_C and high piezoelectricity in BFO-based systems.

Summary of novel conclusions

Our results demonstrate that constructing morphotropic phase boundaries via considering simultaneously the role of lattice distortion might be an effective route to realize both high-temperature and high piezoelectricity in $BiFeO_3$ -based systems.

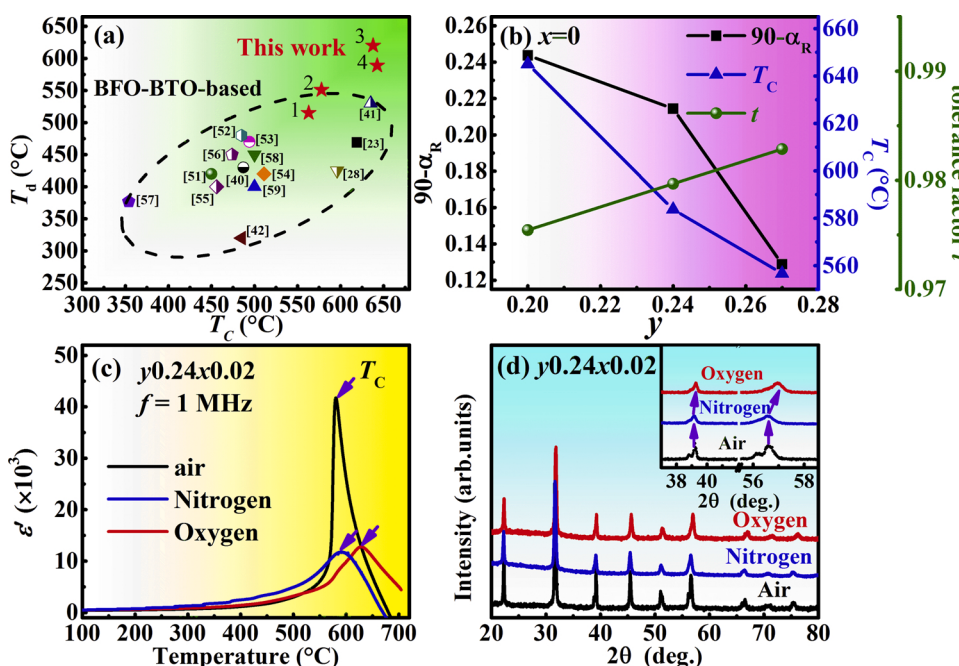


Fig. 8. (a) The relationships between the depolarization temperature T_d and Curie temperature T_C of the reported BFO-BTO based piezoelectric ceramics [23,28,40–4251–59]. 1 represents the $y0.27x0.01$ sample, 2 represents the $y0.24x0.02$ sample, 3 represents the $y0.24x0.01$ sample, 4 represents the $y0.2x0.01$ sample. (b) The y dependent R distortion (characterized by $90-\alpha_R$) and tolerance factor t by fixing $x = 0$ for the samples lying in the R phase region. (c) The temperature dependence of dielectric constant ϵ' at $f = 1$ MHz for the $y0.24x0.02$ sample sintered in air, N_2 and O_2 . (d) The RT XRD patterns of $y0.24x0.02$ sample sintered in air, N_2 and O_2 . Inset in (d) is corresponding magnification around 39 ° and 57 °.

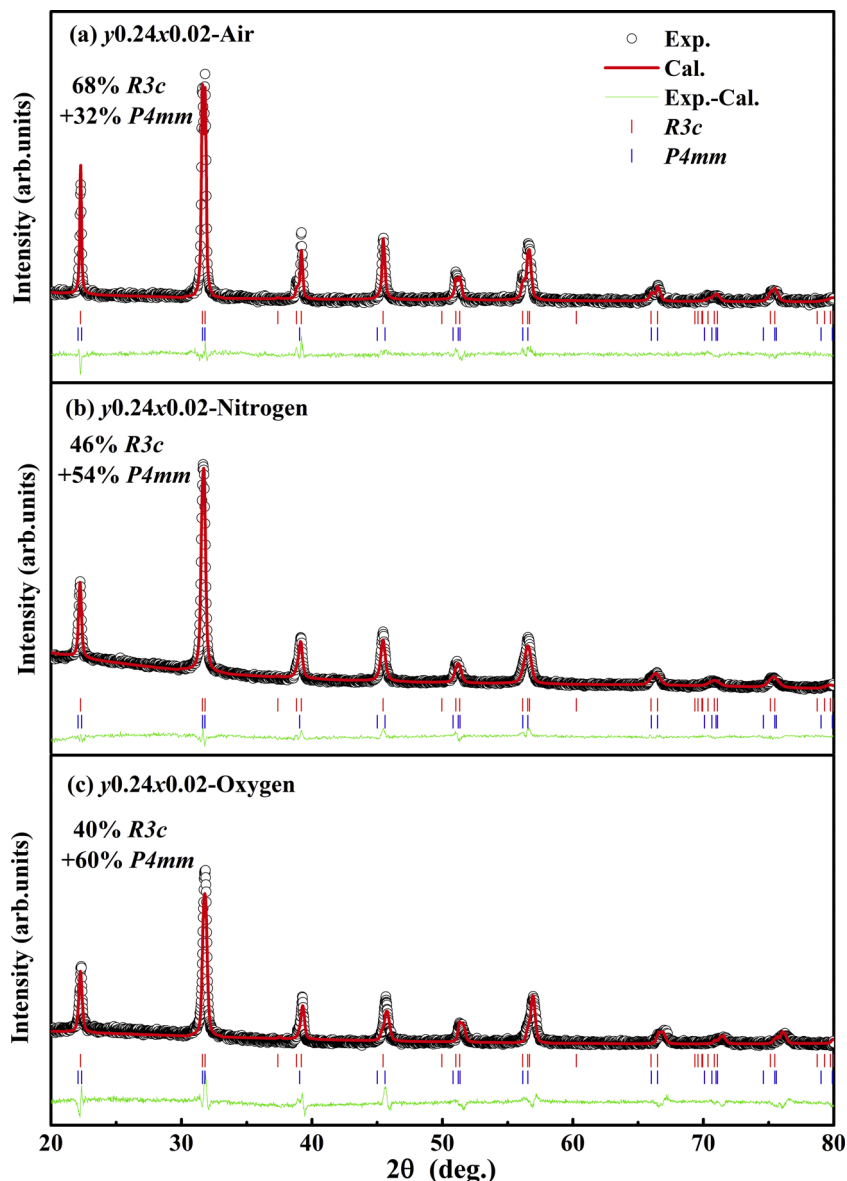


Fig. 9. The Rietveld analysis results of RT XRD patterns for the $y_{0.24}x_{0.02}$ sample sintered in (a) air, (b) N_2 and (c) O_2 .

Declaration of Competing Interest

The authors declare that they have no conflicts of interest.

Acknowledgments

This work was supported by the National Natural Science Foundation of China under Grant No. 11874360, Key Research Program of Frontier Sciences, Chinese Academy of Sciences (QYZDB-SSW-SLH015), and the Joint Funds of the National Natural Science Foundation of China and the Chinese Academy of Sciences Large-Scale Scientific Facility under Grant No. U1832115.

Appendix A. Supplementary data

Supplementary material related to this article can be found, in the online version, at doi:<https://doi.org/10.1016/j.jeurceramsoc.2021.8.030>.

References

- [1] B. Jaffe, W.R. Cook, H. Jaffe, *Piezoelectric Ceramics*, Academic Press, London, 1971.
- [2] J.G. Wu, Perovskite lead-free piezoelectric ceramics, *J. Appl. Phys.* 127 (2020), 190901.
- [3] J. Rodel, K.G. Webber, R. Dittmer, W. Jo, M. Kimura, D. Damjanovic, Transferring lead-free piezoelectric ceramics into application, *J. Eur. Ceram. Soc.* 35 (2015) 1659–1681.
- [4] X.D. Zhang, H.X. Yan, M.J. Reece, Effect of A site substitution on the properties of $CaBi_2Nb_2O_9$ ferroelectric ceramics, *J. Am. Ceram. Soc.* 91 (2008) 2928–2932.
- [5] S.J. Zhang, F.P. Yu, Piezoelectric materials for high temperature sensors, *J. Am. Ceram. Soc.* 94 (2011) 3153–3170.
- [6] J. Wu, J.F. Zhou, J.Y. Song, D. Wang, X.B. Zhu, Y.P. Sun, L.H. Yin, W.H. Song, Evolution of structure, magnetism and ferroelectricity in the $(1-x)BiFeO_3-xBa_{0.5}Sr_{0.5}MnO_3(0 \leq x \leq 1)$ solid solutions, *J. Alloys. Compd.* 774 (2019) 515–521.
- [7] T.P. Comyn, S.P. McBride, A.J. Bell, Processing and electrical properties of $BiFeO_3-PbTiO_3$ ceramics, *Mater. Lett.* 58 (2004) 3844–3846.
- [8] A.J. Bell, T.P. Comyn, T.J. Stevenson, Expanding the application space for piezoelectric materials, *APL Mater.* 9 (2021), 010901.
- [9] J.E. Garcia, F. Rubio-Marcos, Polymorphic phase boundary in piezoelectric oxides, *J. Appl. Phys.* 127 (2020) 131102.
- [10] Z.M. Fan, S.J. Zhang, X.L. Tan, Phase-composition dependent domain responses in $(K_{0.5}Na_{0.5})NbO_3$ -based piezoceramics, *J. Eur. Ceram. Soc.* 40 (2020) 1217–1222.

- [11] X. Lv, Y.B. Chen, B. Wu, J.G. Zhu, D.Q. Xiao, J. Wu, An alternative way to enhance piezoelectricity and temperature stability in lead-free sodium niobate piezoceramics, *Inorg. Chem.* 57 (2018) 10383–10389.
- [12] J. Ma, J. Wu, B. Wu, W.J. Wu, Advances in the modification of the contradictory relationship between piezoelectricity and Curie temperature: simultaneous realization of large piezoelectricity and high Curie temperature in potassium sodium niobate-based ferroelectrics, *J. Mater. Chem. C* 8 (2020) 9506–9510.
- [13] J. Wu, G.C. Zhao, Z.Z. Jiang, D. Wang, J. Yang, P. Tong, X.B. Zhu, L.H. Yin, W. H. Song, Y.P. Sun, Structural, piezoelectric, multiferroic and magnetoelectric properties of $(1-x)$ BiFeO₃- x Ba_{1-y}Sr_yTiO₃(3)solid solutions, *J. Electroceram.* 44 (2020) 256–264.
- [14] M.H. Lee, D.J. Kim, J.S. Park, S.W. Kim, T.K. Song, M.H. Kim, W.J. Kim, D. Do, I. K. Jeong, High-performance lead-free piezoceramics with high curie temperatures, *Adv. Mater.* 27 (2015) 6976–6982.
- [15] A. Singh, C. Moriyoshi, Y. Kuroiwa, D. Pandey, Evidence for local monoclinic structure, polarization rotation, and morphotropic phase transitions in $(1-x)$ BiFeO₃- x BaTiO₃ solid solutions: a high-energy synchrotron x-ray powder diffraction study, *Phys. Rev. B* 88 (2013) 6982.
- [16] G. Wang, Z.M. Fan, S. Murakami, Z.L. Lu, D.A. Hall, D.C. Sinclair, A. Feteira, X. L. Tan, J.L. Jones, A.K. Kleppe, D.W. Wang, I.M. Reaney, Origin of the large electrostrain in BiFeO₃-BaTiO₃ based lead-free ceramics, *J. Mater. Chem. A* 7 (2019) 21254–21263.
- [17] T. Zheng, J.G. Wu, D.Q. Xiao, J.G. Zhu, Recent development in lead-free perovskite piezoelectric bulk materials, *Prog. Mater. Sci.* 98 (2018) 552–624.
- [18] G.L. Yuan, S.W. Or, H.L.W. Chan, Structural transformation and ferroelectric-paraelectric phase transition in $Bi_{1-x}La_xFeO_3$ ($x=0-0.25$) multiferroic ceramics, *J. Phys. D Appl. Phys.* 40 (2007) 1196–1200.
- [19] L.F. Zhu, B.P. Zhang, J.Q. Duan, B.W. Xun, N. Wang, Y.C. Tang, G.L. Zhao, Enhanced piezoelectric and ferroelectric properties of BiFeO₃-BaTiO₃ leadfree ceramics by optimizing the sintering temperature and dwell time, *J. Eur. Ceram. Soc.* 38 (2018) 3463–3471.
- [20] M. El-Saadawy, Diffusion coefficient of vacancies and jump length of electrons in $Co_{1-x}Zn_xFe_2O_4$ ferrites, *J. Adv. Ceram.* 1 (2012) 144–149.
- [21] M.N. Rahaman, *Ceramic Processing and Sintering*, CRC Press, Boca Raton, 2003.
- [22] Y.X. Liu, Z. Li, H.C. Thong, J.T. Lu, J.F. Li, W. Gong, K. Wang, Grain size effect on piezoelectric performance in perovskite-based piezoceramics, *Acta Phys. Sin.* 69 (2020), 217704.
- [23] S.O. Leontsev, R.E. Eitel, Dielectric and piezoelectric properties in Mn-Modified $(1-x)$ BiFeO₃- x BaTiO₃ ceramics, *J. Am. Ceram. Soc.* 92 (2009) 2957–2961.
- [24] G. Catalan, Magnetocapacitance without magnetoelectric coupling, *Appl. Phys. Lett.* 88 (2006), 102902.
- [25] I. Calisir, A.A. Amirov, A.K. Kleppe, D.A. Hall, Optimisation of functional properties in lead-free BiFeO₃-BaTiO₃ ceramics through La³⁺ substitution strategy, *J. Mater. Chem. A* 6 (2018) 5378–5397.
- [26] I. Calisir, A.K. Kleppe, A. Feteira, D.A. Hall, Quenching-assisted actuation mechanisms in core-shell structured BiFeO₃-BaTiO₃ piezoceramics, *J. Mater. Chem. C* 7 (2019) 10218–10230.
- [27] Q.Q. Ke, X.J. Lou, Y. Wang, J. Wang, Oxygen-vacancy-related relaxation and scaling behaviors of $Bi_{0.9}La_{0.1}Fe_{0.98}Mg_{0.02}O_3$ ferroelectric thin films, *Phys. Rev. B* 82 (2010), 024102.
- [28] Y.Q. Guo, P. Xiao, R. Wen, Y. Wan, Q.J. Zheng, D.L. Shi, K.H. Lam, M.L. Liu, D. M. Lin, Critical roles of Mn-ions in enhancing the insulation, piezoelectricity and multiferroicity of BiFeO₃-based lead-free high temperature ceramics, *J. Mater. Chem. C* 3 (2015) 5811–5824.
- [29] X.P. Wang, J.G. Wu, D.Q. Xiao, X.J. Cheng, T. Zheng, X.J. Lou, B.Y. Zhang, J. G. Zhu, New potassium-sodium niobate ceramics with a giant d_{33} , *ACS Appl. Mater. Inter.* 6 (2014) 6177–6180.
- [30] C.A. Randall, N. Kim, J.P. Kucera, W.W. Cao, T.R. Shroud, Intrinsic and extrinsic size effects in fine-grained morphotropic-phase-boundary lead zirconate titanate ceramics, *J. Am. Ceram. Soc.* 81 (1998) 677–688.
- [31] J. Bennett, T.R. Shroud, S.J. Zhang, P. Mandal, A.J. Bell, T.J. Stevenson, T. P. Comyn, Temperature dependence of the intrinsic and extrinsic contributions in BiFeO₃- $(K_{0.5}Bi_{0.5})TiO_3$ -PbTiO₃ piezoelectric ceramics, *J. Appl. Phys.* 116 (2014), 094102.
- [32] F. Li, D.B. Lin, Z.B. Chen, Z.X. Cheng, J.L. Wang, C.C. Li, Z. Xu, Q.W. Huang, X. Z. Liao, L.Q. Chen, T.R. Shroud, S.J. Zhang, Ultrahigh piezoelectricity in ferroelectric ceramics by design, *Nat. Mater.* 17 (2018) 349–354.
- [33] W.F. Liu, X.B. Ren, Large piezoelectric effect in Pb-Free ceramics, *Phys. Rev. Lett.* 103 (2009) 257602.
- [34] X.P. Wang, J.G. Wu, D.Q. Xiao, J.G. Zhu, X.J. Cheng, T. Zheng, B.Y. Zhang, X. J. Lou, X.J. Wang, Giant Piezoelectricity in Potassium-Sodium Niobate Lead-Free Ceramics, *J. Am. Chem. Soc.* 136 (2014) 2905–2910.
- [35] K. Xu, J. Li, X. Lv, J.G. Wu, X.X. Zhang, D.Q. Xiao, J.G. Zhu, Superior piezoelectric properties in potassium-sodium niobate lead-free ceramics, *Adv. Mater.* 28 (2016) 8519–8523.
- [36] D.M. Lin, K.W. Kwok, Structure, ferroelectric, and piezoelectric properties of $(Bi_{0.5}Na_{0.5})_{1-x-y} (Bi_{0.5}K_{0.5})_x Ba_y Sr_z TiO_3$ lead-free ceramics, *J. Am. Ceram. Soc.* 93 (2010) 806–813.
- [37] G.F. Fan, W.Z. Lu, X.H. Wang, F. Liang, Morphotropic phase boundary and piezoelectric properties of $(Bi_{1/2}Na_{1/2})TiO_3$ - $(Bi_{1/2}K_{1/2})TiO_3$ -KNbO₃ lead-free piezoelectric ceramics, *Appl. Phys. Lett.* 91 (2007), 202908.
- [38] B.W. Xun, N. Wang, B.P. Zhang, X.Y. Chen, Y.Q. Zheng, W.S. Jin, R. Mao, K. Liang, Enhanced piezoelectric properties of $0.7BiFeO_3-0.3BaTiO_3$ lead-free piezoceramics with high Curie temperature by optimizing Bi self-compensation, *Ceram. Int.* 45 (2019) 24382–24391.
- [39] J.G. Chen, J.R. Cheng, Enhanced thermal stability of lead-free high temperature $0.75BiFeO_3-0.25BaTiO_3$ ceramics with excess Bi content, *J. Alloys. Compd.* 589 (2014) 115–119.
- [40] J.X. Wei, D.Y. Fu, J.R. Cheng, J.G. Chen, Temperature dependence of the dielectric and piezoelectric properties of $xBiFeO_3-(1-x)BaTiO_3$ ceramics near the morphotropic phase boundary, *J. Mater. Sci.* 52 (2017) 10726–10737.
- [41] J.G. Chen, J.R. Cheng, J.L. Guo, Z.X. Cheng, J.L. Wang, H.B. Liu, S.J. Zhang, Excellent thermal stability and aging behaviors in BiFeO₃-BaTiO₃ piezoelectric ceramics with rhombohedral phase, *J. Am. Ceram. Soc.* 103 (2020) 374–381.
- [42] T. Zheng, J.G. Wu, Perovskite BiFeO₃-BaTiO₃ ferroelectrics: engineering properties by domain evolution and thermal depolarization modification, *Adv. Electron. Mater.* 6 (2020) 2000079.
- [43] M. Alguero, P. Ramos, R. Jimenez, H. Amorin, E. Vila, A. Castro, High temperature piezoelectric BiScO₃-PbTiO₃ synthesized by mechanochemical methods, *Acta Mater.* 60 (2012) 1174–1183.
- [44] J. Bennett, A.J. Bell, T.J. Stevenson, T.P. Comyn, Tailoring the structure and piezoelectric properties of BiFeO₃- $(K_{0.5}Bi_{0.5})TiO_3$ -PbTiO₃ ceramics for high temperature applications, *Appl. Phys. Lett.* 103 (2013), 152901.
- [45] T. Leist, W. Jo, T. Comyn, A. Bell, J. Rodel, Shift in morphotropic phase boundary in La-Doped BiFeO₃-PbTiO₃ piezoceramics, *J. Appl. Phys.* 48 (2009), 120205.
- [46] C.M. Wang, S.J. Zhang, J.F. Wang, M.L. Zhao, C.L. Wang, Electromechanical properties of calcium bismuth niobate ($CaBi_2Nb_2O_9$) ceramics at elevated temperature, *Mater. Chem. Phys.* 118 (2009) 21–24.
- [47] X.P. Jiang, Q. Yang, S.L. Zhou, C. Chen, Y. Chen, N. Tu, Z.D. Yu, Microstructure and properties of high-temperature materials $(1-x)Na_{0.5}Bi_{2.5}Nb_2O_9-xLiNbO_3$, *J. Am. Ceram. Soc.* 94 (2011) 1109–1113.
- [48] C.M. Wang, J.F. Wang, Aurivillius phase potassium bismuth titanate: $K_0.5Bi_{4.5}Ti_{15}$, *J. Am. Ceram. Soc.* 91 (2008) 918–923.
- [49] C.C. Huang, K. Cai, Y.C. Wang, Y. Bai, D. Guo, Revealing the real high temperature performance and depolarization characteristics of piezoelectric ceramics by combined in situ techniques, *J. Mater. Chem. C* 6 (2018) 1433–1444.
- [50] D. Damjanovic, Ferroelectric, dielectric and piezoelectric properties of ferroelectric thin films and ceramics, *Rep. Prog. Phys.* 61 (1998) 1267–1324.
- [51] Z.Y. Cen, C.R. Zhou, H.B. Yang, Q. Zhou, W.Z. Li, C.L. Yan, L. Cao, J. Song, L. Peng, Remarkably high-temperature stability of $Bi(Fe_{1-x}Al_x)O_3$ -BaTiO₃ solid solution with near-zero temperature coefficient of piezoelectric properties, *J. Am. Ceram. Soc.* 96 (2013) 2252–2256.
- [52] H.B. Yang, C.R. Zhou, X.Y. Liu, Q. Zhou, G.H. Chen, W.Z. Li, H. Wang, Piezoelectric properties and temperature stabilities of Mn- and Cu-modified BiFeO₃-BaTiO₃ high temperature ceramics, *J. Eur. Ceram. Soc.* 33 (2013) 1177–1183.
- [53] Q.L. Fan, C.R. Zhou, Q.L. Li, J.W. Xu, C.L. Yuan, G.H. Chen, Temperature stability of sodium-doped BiFeO₃-BaTiO₃ piezoelectric ceramics, *J. Mater. Sci.-Mater. El.* 26 (2015) 9336–9341.
- [54] Y.X. Wei, C.Q. Jin, Y.M. Zeng, X.T. Wang, G. Xu, X.L. Wang, Polar order evolutions near the rhombohedral to Pseudocubic and Tetragonal to pseudocubic phase boundaries of the BiFeO₃-BaTiO₃ system, *Materials* 8 (2015) 8355–8365.
- [55] J.G. Chen, J.R. Cheng, High electric-induced strain and temperature-dependent piezoelectric properties of $0.75BF-0.25BZT$ lead-free ceramics, *J. Am. Ceram. Soc.* 99 (2016) 536–542.
- [56] K. Tong, C.R. Zhou, J. Wang, Q.N. Li, L. Yang, J.W. Xu, W.D. Zeng, G.H. Chen, C. L. Yuan, G.H. Rao, Enhanced piezoelectricity and high-temperature sensitivity of Zn-modified BF-BT ceramics by in situ and ex situ measuring, *Ceram. Int.* 43 (2017) 3734–3740.
- [57] Y.X. Wei, J.H. Shen, C.X. Bai, C.Q. Jin, W.T. Zhu, Y. Tian, Z.H. Dai, G. Xu, Nature of polar state in $0.67BiFeO_3-0.33BaTiO_3$, *J. Mater. Sci.-Mater. El.* 31 (2020) 19266–19276.
- [58] Z. Yu, J.T. Zeng, L.Y. Zheng, W.B. Liu, G.R. Li, A. Kassiba, Large piezoelectricity and high Curie temperature in novel bismuth ferrite-based ferroelectric ceramics, *J. Am. Ceram. Soc.* 103 (2020) 6435–6444.
- [59] T. Zheng, Z.G. Jiang, J.G. Wu, Enhanced piezoelectricity in $(1-x)Bi_{1.05}Fe_{1-y}Al_yO_3$ - x BaTiO₃ lead-free ceramics: site engineering and wide phase boundary region, *Dalton Trans.* 45 (2016) 11277–11285.
- [60] R.E. Eitel, C.A. Randall, T.R. Shroud, P.W. Rehrig, W. Hackenberger, S.E. Park, New high temperature morphotropic phase boundary piezoelectrics based on Bi(Me)₃-PbTiO₃ ceramics, *J. Appl. Phys.* 1 (40) (2001) 5999–6002.